

Supplementary Information

Ideal trigonal prismatic coordination geometry of Co(II) in a honeycomb MOF with a triptycene-based ligand

Yoshiaki Shuku,^a Rie Suizu,^{a,b} Masahisa Tsuchiizu,^{*c} and Kunio Awaga^{*a}

^a Department of Chemistry & Integrated Research Consortium on Chemical Sciences (IRCCS), Nagoya University, Furo-cho, Chikusa-ku, Nagoya 464-8602, Japan.

^b Japan Science and Technology Agency (JST), PRESTO, 4-1-8 Honcho, Kawaguchi, Saitama 332-0012, Japan

^c Department of Physics, Nara Women's University, Kitauoyanishi-machi, Nara 630-8506, Japan.

1. Synthesis of [Co(<i>o</i>-TT)]·3CH₃CN	S2
2. Crystal structure analysis of [Co(<i>o</i>-TT)]·3CH₃CN	S3
3. Theoretical model calculation for the magnetic anisotropy of Co(II) ion in trigonal prismatic coordination geometry	S8
4. Magnetic data for [Co(<i>o</i>-TT)]·3CH₃CN	S12
5. Powder X-ray diffraction data for polycrystalline sample	S15

1. Synthesis of $[\text{Co}(o\text{-TT})] \cdot 3\text{CH}_3\text{CN}$

The crystals of $[\text{Co}(o\text{-TT})]$ were prepared by the procedures, carried out under an N_2 atmosphere. An acetonitrile (MeCN) solution of $\text{Co}_2(\text{CO})_8$ (~20 mg) and a small glass tube with a DMF suspension of $o\text{-TT}$ (~20 mg) and dry CoCl_2 (~1 mg), were placed in a 10 ml vial (see Fig. S1), keeping the reactants apart. Note that we empirically found that the redox reaction between neutral $o\text{-TT}$ and $\text{Co}_2(\text{CO})_8$ produced better quality crystals of $[\text{Co}(o\text{-TT})] \cdot 3\text{CH}_3\text{CN}$ with the presence of a small amount of CoCl_2 . Then, acetonitrile was slowly poured to fill the vial and let the diffusion of reactants start. The lid of the vial was closed during slow diffusion crystallization. Within a month, the black crystals of $[\text{Co}(o\text{-TT})] \cdot 3\text{CH}_3\text{CN}$ were grown in the glass tube.

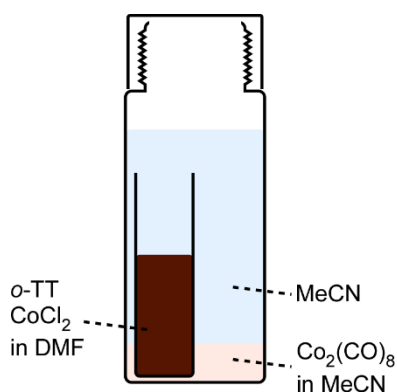


Figure S1. Apparatus for the crystal growth of $[\text{Co}(o\text{-TT})] \cdot 3\text{CH}_3\text{CN}$.

2. Crystal structure analysis of [Co(*o*-TT)]·3CH₃CN

The X-ray diffraction data for single crystal structure analysis were collected on a Rigaku AFC-10 instrument equipped with a MicroMax-007 microfocus rotating anode X-ray generator by using graphite-monochromated Mo K α radiation ($\lambda = 0.71073 \text{ \AA}$) and a HyPix6000 hybrid photon counting detector under a cold nitrogen stream. The frame data were integrated and corrected for absorption with the Rigaku Oxford Diffraction CrysAlisPro package.^{S1} The crystal structure was solved using intrinsic phasing methods (SHELXT-2018/2)^{S2} and standard difference map techniques and refined by full-matrix least-square procedures on F^2 (SHELXL-2018/3).^{S3} All non-hydrogen atoms were refined anisotropically. All hydrogen atoms were placed at calculated positions and refined using a riding model. All calculations were performed using the OlexSys Olex2 crystallographic software package.^{S4} Details of the crystal data and a summary of the intensity data collection parameters of X-ray crystallography are listed in Table S1.

We concluded with the *Pbca* space group, though the ADDSYM in PLATON program^{S5} suggested a more symmetric space group *Cmcm* with a unit cell half the size of that in *Pbca* as an alternative. This is because the intensity of the diffraction peaks attributed to $l = 2n+1$ is weak due to the disordered solvents in void spaces. After analysis with the *Pbca* space group, there was a large residual electron density around Co atom derived from the disordering solvent molecules. Following this, we also performed the analysis without solvents disordered in the void spaces using the SQUEEZE subroutine in PLATON. Since there were no significant extinction rules in the *a*- and *c*-axis directions, the space group was determined to be *Cmcm*. There was no large residual electron density around Co atom, and no difference in the bond lengths or angles of the honeycomb network formed by Co ions and *o*-TT ligands with or without solvent (Table S2). According to these analyses, we discussed the crystals structures based on the result with crystal solvents in main text.

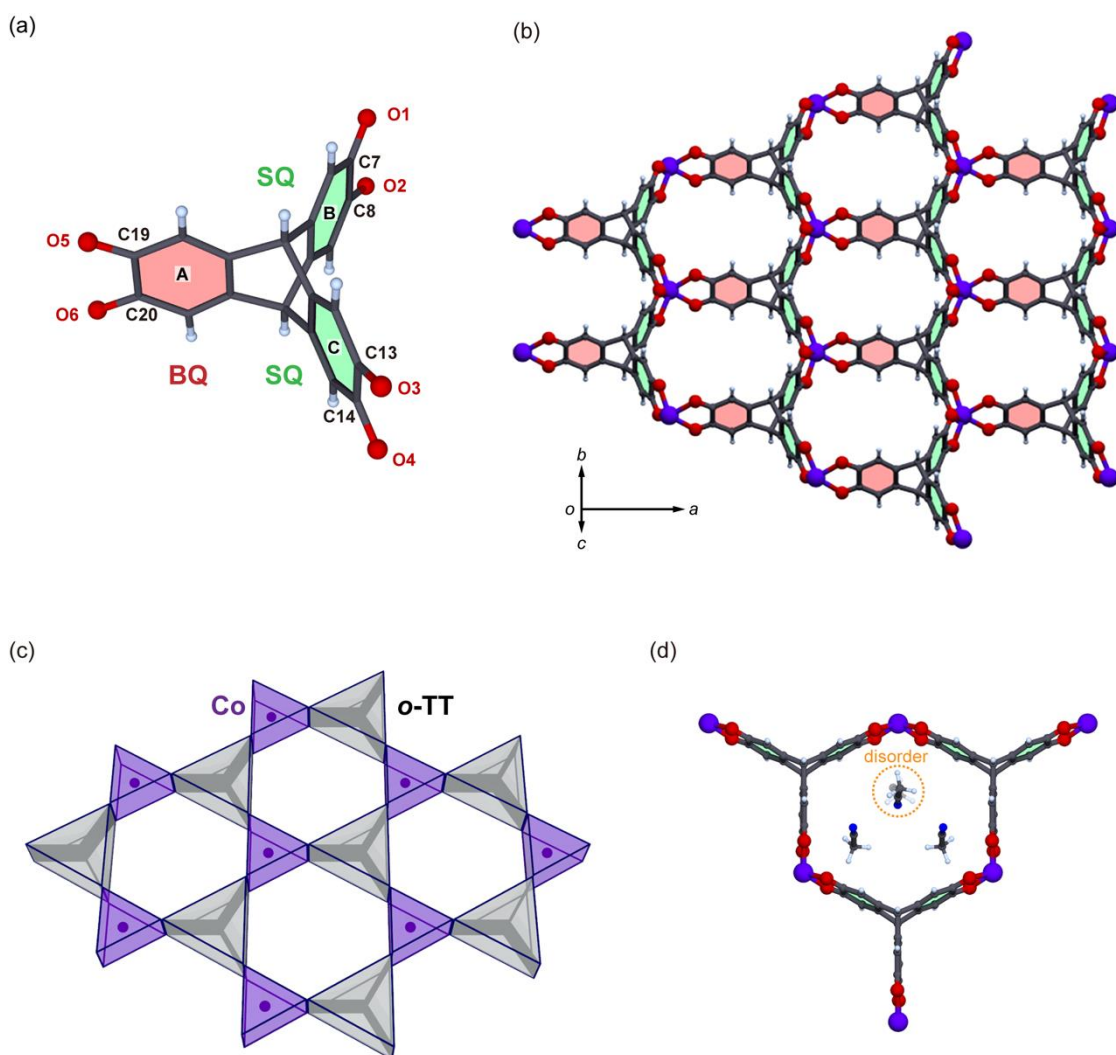


Fig. S2. (a) Molecular structure of *o*-TT moiety, (b) honeycomb structure of [Co(*o*-TT)]·3CH₃CN, (c) the 2D network structure formed by two kinds of the trigonal prism of Co moiety and *o*-TT, and (d) the arrangement of the crystal solvent molecules. The disordered solvent molecules are marked with an orange dotted circle.

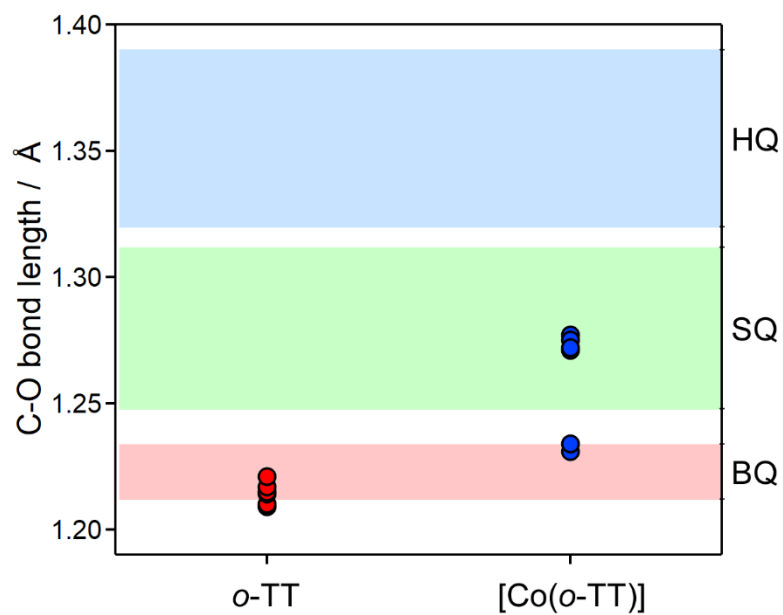


Fig. S3. Comparison of the C–O bond distances of quinone molecules. Red and blue circles show the C–O bond lengths of neutral *o*-TT and [Co(*o*-TT)], respectively. The blue, green and red regions show the range of C–O bond distances for HQ, SQ and BQ metal complexes reported in references.^{S6}

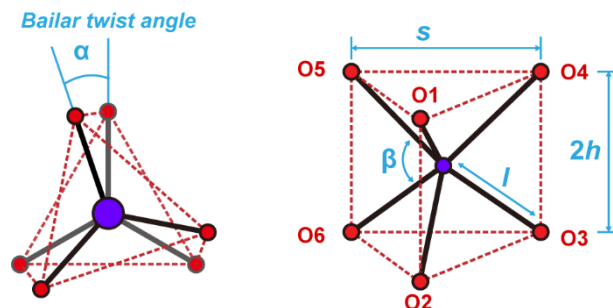
Table S1. Crystallographic Data for [Co(*o*-TT)]·3CH₃CN and [Co(*o*-TT)] (squeezed).

	[Co(<i>o</i> -TT)]·3CH ₃ CN	[Co(<i>o</i> -TT)] (squeezed)
CCDC No.	2255851	2281350
formula	C ₂₆ H ₁₇ CoN ₃ O ₆	C ₂₀ H ₈ CoO ₆
fw	526.35	403.19
<i>T</i> (K)	123(2)	123(2)
λ (Å)	0.71073	0.71073
cryst syst	orthorhombic	orthorhombic
space group	<i>Pbca</i>	<i>Cmcm</i>
<i>a</i> (Å)	18.9411(3)	11.6718(2)
<i>b</i> (Å)	11.4350(2)	18.9425(3)
<i>c</i> (Å)	23.3417(4)	11.4351(2)
α (degree)	90	90
β (degree)	90	90
γ (degree)	90	90
<i>V</i> (Å ³)	5055.61(15)	2528.22(7)
<i>Z</i>	8	4
<i>D</i> _{calc} (g / cm ³)	1.383	1.059
μ (mm ⁻¹)	0.724	0.702
<i>F</i> (000)	2152	812
cryst size (mm)	0.25 × 0.06 × 0.03	0.25 × 0.06 × 0.03
θ range (deg)	3.491–27.484	3.669–29.080
reflns collected	150084	41642
indep reflns/ <i>R</i> _{int}	5788 / 0.0372	1854 / 0.0251
params	339	71
GOF on <i>F</i> ²	1.082	1.107
<i>R</i> ₁ ^{<i>a</i>} , <i>wR</i> ₂ ^{<i>b</i>} [<i>I</i> > 2 σ (<i>I</i>)]	0.0754, 0.2452	0.0280, 0.0802
<i>R</i> ₁ ^{<i>a</i>} , <i>wR</i> ₂ ^{<i>b</i>} (all data)	0.0969, 0.2789	0.0285, 0.0802

^{*a*} $R_1 = \frac{\sum ||F_o| - |F_c||}{\sum |F_o|}$. ^{*b*} $wR_2 = [\frac{\sum \{w(F_o^2 - F_c^2)^2\}}{\sum w(F_o^2)^2}]^{1/2}$.

^{*c*} $S = [\frac{\sum \{w(F_o^2 - F_c^2)^2\}}{(N_{\text{ref}} - N_{\text{par}})}]^{1/2}$

Table S2. Selected distances and angles for [Co(*o*-TT)]·3CH₃CN and [Co(*o*-TT)] (squeezed).



	[Co(<i>o</i> -TT)]·3CH ₃ CN	[Co(<i>o</i> -TT)] (Squeezed)
<u>Bailar twist angles α (°)</u>		
α_{O1-O2}	0.63	0 ^a
α_{O3-O4}	0.33	0 ^a
α_{O5-O6}	0.35	0 ^a
<u>Cobalt-O distances l (Å)</u>		
Co-O1	2.052(2)	} 2.0475(8) ^b
Co-O2	2.051(2)	
Co-O3	2.047(2)	
Co-O4	2.047(2)	
Co-O5	2.127(2)	} 2.1274(11) ^b
Co-O6	2.132(2)	
<u>Trigonal side distances s (Å)</u>		
O1-O4	2.853	} 2.863 ^b
O2-O3	2.891	
O1-O5	2.755	} 2.750 ^b
O2-O6	2.741	
O4-O5	2.767	
O3-O6	2.747	
<u>Trigonal bite distances $2h$ (Å)</u>		
O1-O2	2.615	} 2.615 ^b
O3-O4	2.614	
O5-O6	2.587	2.584
<u>Bite angles β (°)</u>		
O1-Co-O2	79.19	} 79.37 ^b
O3-Co-O4	79.35	
O5-Co-O6	74.79	74.70

^a Symmetry requirement (mirror planes), ^b Symmetry equivalence.

3. Theoretical model calculation for the magnetic anisotropy of the Co(II) ion in trigonal prismatic coordination geometry

The magnetic anisotropy was examined based on the isolated Co(II) ion in the trigonal prism. The structure geometry is shown in Fig. S4a, where l is the bond distance between the Co site and the O site, and h is the height. The crystal-electric field (CEF) potential around the Co center due to the oxygen sites can be evaluated from the conventional expansion of the Coulomb potential

$$H'_{D_{3h}} = (Ar^2 + A'r^4) \cos 2\theta - Br^3(3 \sin \theta - \sin 3\theta) \sin 3\phi - Cr^4 \cos 4\theta$$

where r is the radial coordinate, θ is the polar angle, and ϕ is the azimuthal angle, and

$$A \equiv \frac{9(2h^2 - a^2)Ze^2}{4l^5},$$

$$A' \equiv -\frac{Ze^2}{4\pi\epsilon_0} \frac{15(24a^2h^2 - 3a^4 - 8h^4)}{64l^9},$$

$$B \equiv \frac{15a^3Ze^2}{16l^7},$$

$$C \equiv \frac{Ze^2}{4\pi\epsilon_0} \frac{105(24a^2h^2 - 3a^4 - 8h^4)}{256l^9}.$$

Here Z is the atomic number, and a , h , and l are the structural parameters defined in the inset of Fig. S4a. Here we note that these parameters can change their signs depending on the structure of the trigonal prism. The lowest contribution is the A term, which would take a small value for the geometry of the present [Co(*o*-TT)] with $2h^2 = 3.5 \text{ \AA}^2$ and $a^2 = 2.7 \text{ \AA}^2$.

By taking the average over the radial coordinates and by using the hydrogenic radial wavefunction, the effective potential is given by

$$H_{D_{3h}}^{\text{eff}} = \Delta \cos 2\theta - \Delta' \cos 4\theta$$

where Δ and Δ' are defined by

$$\Delta = A \int_0^\infty dr R_{3,2}^*(r) r^4 R_{3,2}(r) - A' \int_0^\infty dr R_{3,2}^*(r) r^6 R_{3,2}(r)$$

$$\Delta' = C \int_0^\infty dr R_{3,2}^*(r) r^6 R_{3,2}(r)$$

Here $R_{32}(r)$ is the hydrogenic radial wavefunction of the 3d orbital, and Z is the atomic number. The azimuthal angle dependent B term ($\propto \sin 3\phi$) does not give rise to energy splitting since all the matrix elements are based on the spherical wave function $Y_{l,m}$. The eigenvalues are given by

$$E_{a'_1} = \frac{1}{21}(+\Delta - 5\Delta') \quad (\text{unique } a'_1 (d_{3z^2-r^2}))$$

$$E_{e''} = \frac{1}{21}(-3\Delta + 11\Delta') \quad (\text{doubly degenerate } e'' (d_{xz}, d_{yz}))$$

$$E_{e'} = \frac{1}{21}(-15\Delta - 5\Delta') \quad (\text{doubly degenerate } e' (d_{xy}, d_{x^2-y^2}))$$

The energy splitting on the plane of Δ and Δ' are shown in Fig.S4c.

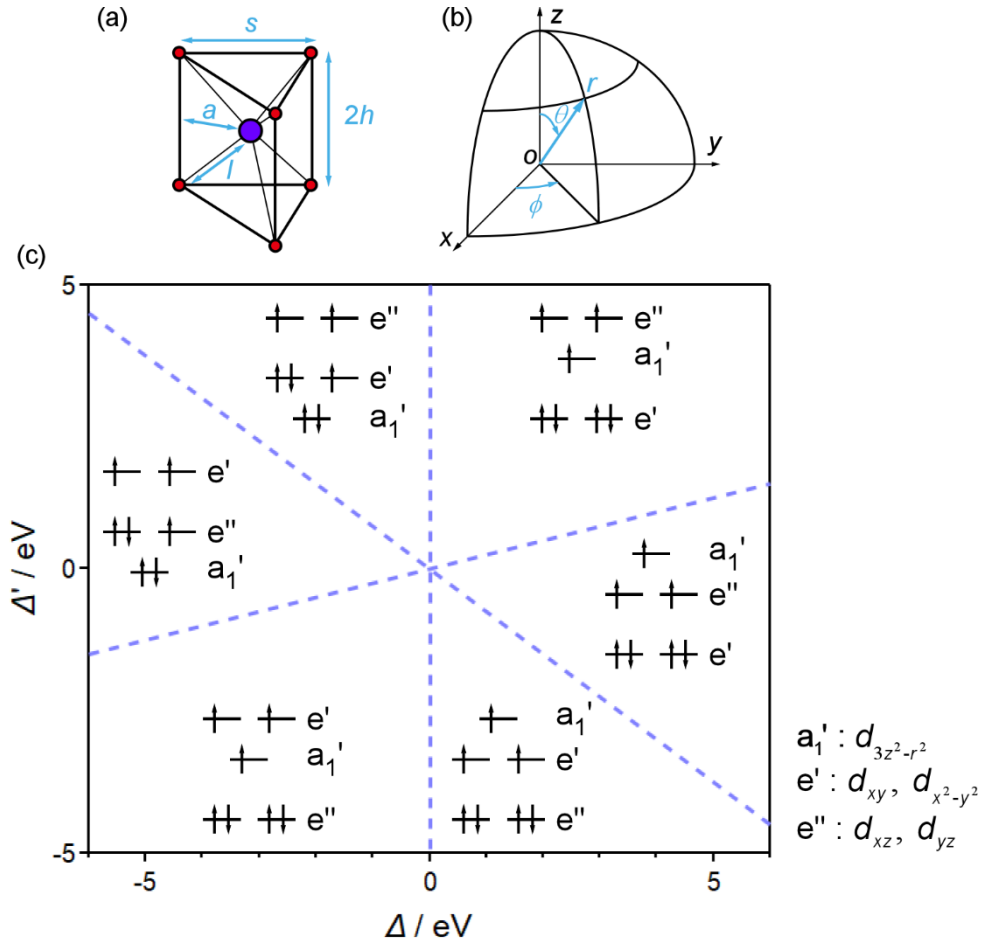


Figure S4. (a) Coordination geometry and the definition structural parameters. (b) Definition of spherical coordination. (c) Diagram of the d orbital energy splittings with the parameters of Δ and Δ' .

The electronic states were evaluated by the standard multi-orbital Hubbard model. The Hamiltonian is given in the second-quantization basis by

$$H_{\text{Hubbard}} = U \sum_{\alpha} n_{\alpha,\uparrow} n_{\alpha,\downarrow} + U' \sum_{\alpha \neq \beta} n_{\alpha,\uparrow} n_{\beta,\downarrow} + \frac{1}{2} (U' - J) \sum_{\alpha \neq \beta} (n_{\alpha,\uparrow} n_{\beta,\uparrow} + n_{\alpha,\downarrow} n_{\beta,\downarrow}) - J \sum_{\alpha \neq \beta} c_{\alpha,\uparrow}^{\dagger} c_{\alpha,\downarrow} c_{\beta,\downarrow}^{\dagger} c_{\beta,\uparrow} + J \sum_{\alpha \neq \beta} c_{\alpha,\uparrow}^{\dagger} c_{\alpha,\downarrow}^{\dagger} c_{\beta,\downarrow} c_{\beta,\uparrow}$$

where $n_{\alpha,\sigma}$ and $c_{\alpha,\sigma}$ are the density and annihilation operators of the electron with orbital α and spin σ . Here the model parameters satisfy $U = U' + 2J$ due to the ion isotropy. The electronic states are examined by the full diagonalization of all the possible configurations of d^7 . The obtained phase diagram of the high-spin and low-spin is shown in Fig. S5. In Fig. S5b, the U value was set as 5 eV which is reasonable value for a transition metal ion.^{S7} Although the estimate of U value is not accurate, the qualitative nature of magnetic anisotropy (Fig. S5b) is universal with different values of U due to the linear relationship between U and Δ (Fig. S5a).

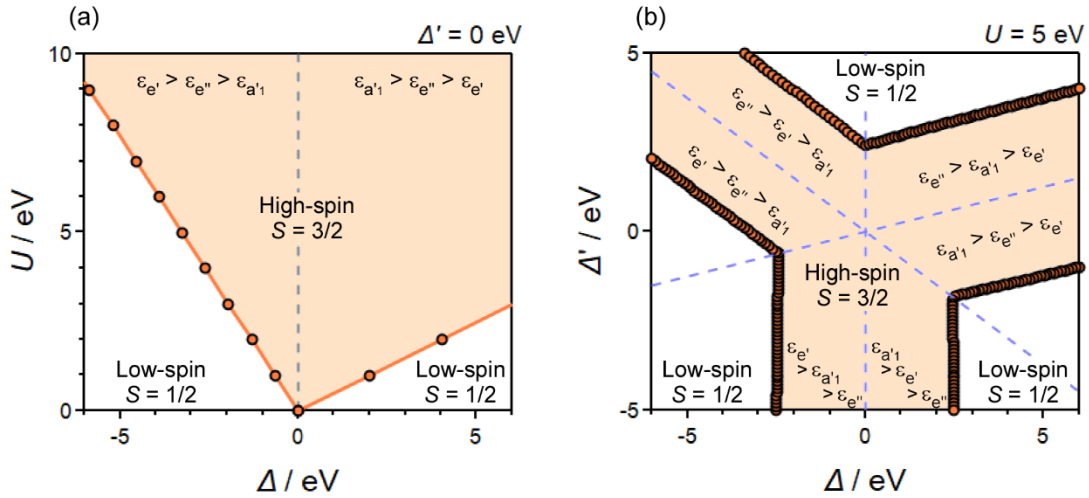


Figure S5. The phase diagram of the high-spin and low-spin states against the parameters of Δ and U with $\Delta' = 0$ eV (a), and against the parameters of Δ and Δ' with $U = 5$ eV (b).

The g -value is evaluated in the standard way^{S8} and is shown in Fig. S6. We observe a drastic change in the g -value anisotropy within the high-spin states. For $\Delta > 0$, both g_z and g_x take values close to 2 with weak anisotropy in g_z/g_x . For $\Delta < 0$, on the other hand, g_x and g_y become zero. Its origin can be attributed to the fact that the a_1' ($d_{3z^2-r^2}$) orbital with the angular momentum $m = 0$ is doubly occupied and does not contribute to magnetic

properties. We also observed discontinuous changes in g_z at $\Delta = -4$ eV and -0.7 eV. The former is due to the transition between high-spin and low-spin states. The latter, which is within the high-spin states, corresponds to the level crossing of the e' and e'' orbital energies.

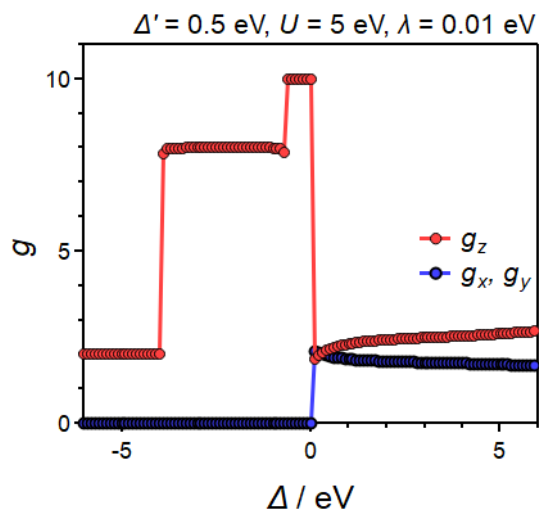


Figure S6. Δ dependence of the g values. The parameters were set as $\Delta' = 0.5$ eV, $U = 5$ eV, $\lambda = 0.01$ eV

4. Magnetic data for [Co(*o*-TT)]·3CH₃CN

Magnetic measurements were carried out on a MPMS-XL Quantum Design magnetometer.

The measurements for polycrystalline sample used a plastic straw as the sample folder. Temperature dependent measurements for polycrystalline sample were performed under 0.1 T in the temperature range of 2–300 K. The temperature dependences of the paramagnetic susceptibilities χ_p were calculated with experimentally obtained diamagnetic susceptibilities by assuming the magnetic contribution follow the Curie-Weiss law at high temperature region.

For the angular dependent measurements, sample of aligned crystals was prepared by fixing thick platelet crystals on a plastic (PVC) plate with Apiezon N grease as shown in Fig. S10. The PVC plate with aligned crystals was fixed on the stage of Horizontal Rotator. Temperature dependent measurements for aligned crystals were performed along three different orientations under 2 T in the temperature range of 2–150 K. The angular dependent measurements of the aligned crystals were performed under 2T at 2, 5, 10, 15, 20 and 25K. The background measurements of rotation apparatus were performed with blank PVC plate and subtracted.

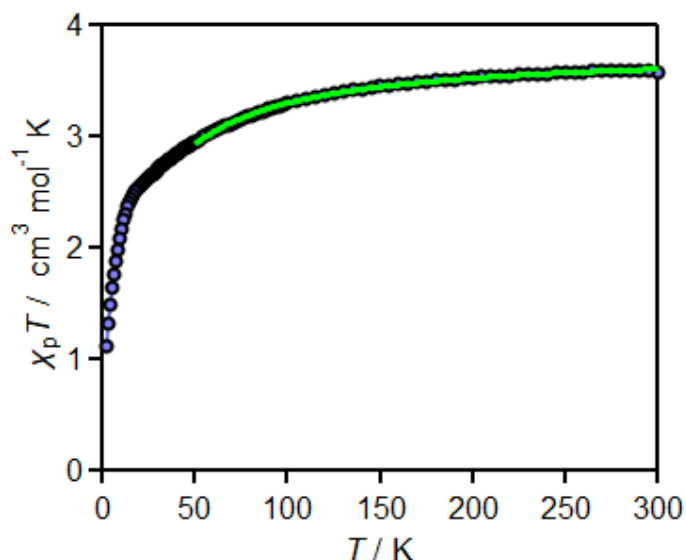


Figure S7. Temperature T dependence of the paramagnetic susceptibility χ_p for polycrystalline [Co(*o*-TT)]. The values of $\chi_p T$ are plotted as a function of T . The green curve shows the theoretical best fit with the Curie-Weiss law.

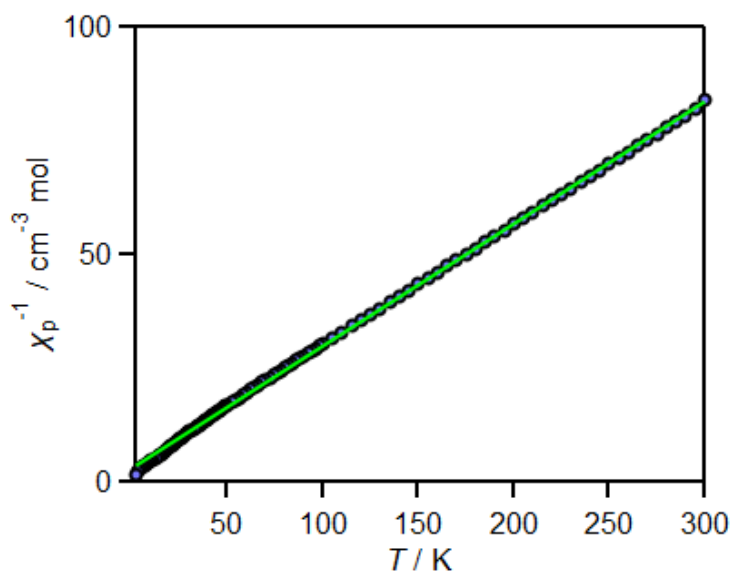


Figure S8. Temperature dependence of the reciprocal paramagnetic susceptibility of polycrystalline [Co(*o*-TT)].

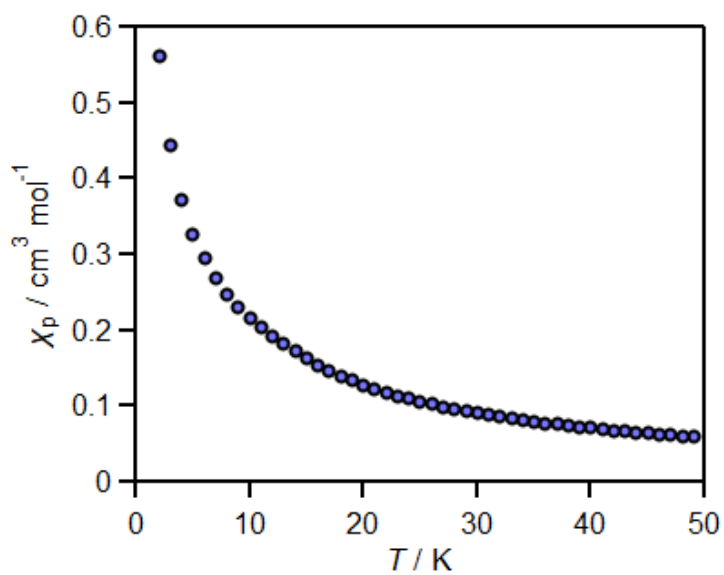


Figure S9. Temperature dependence of the paramagnetic susceptibility of polycrystalline [Co(*o*-TT)] below 50 K.

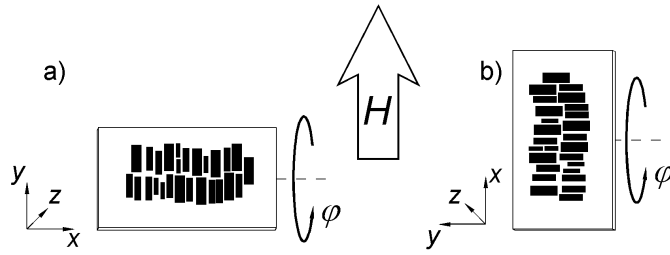


Figure S10. Schematic images of the sample rotation for magnetic anisotropy measurements. Rotation around x axis (a) and y axis. The z axis corresponds to the b axis of the crystal structure. The thick arrow (H) shows the direction of applied magnetic field.

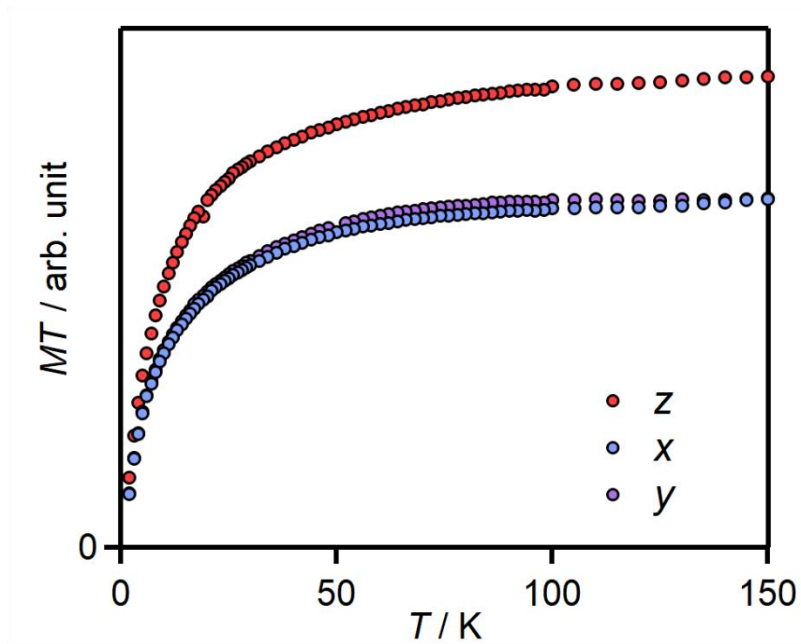


Figure S11. Temperature dependence of M_xT , M_yT and M_zT for aligned crystals of $[\text{Co}(o\text{-TT})]$ below 150 K.

5. Powder X-ray diffraction data for polycrystalline sample

The powder X-ray diffraction (PXRD) data for polycrystalline sample were collected on a Rigaku X-ray diffractometer with a Cu K α radiation ($\lambda = 1.5418 \text{ \AA}$).

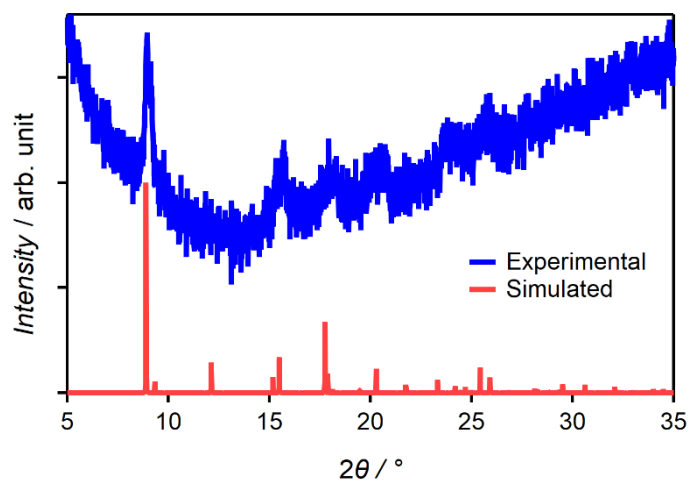


Fig. S12. PXRD pattern of polycrystalline $[\text{Co}(o\text{-TT})]\cdot 3\text{CH}_3\text{CN}$ sample (blue trace). The red trace shows the simulated PXRD pattern of single crystal structure.

References

- S1 CrysAlisPro 1.171.40.67a, (Rigaku Oxford Diffraction, 2019).
- S2 G. M. Sheldrick, *Acta Cryst.*, 2015, **A71**, 3–8.
- S3 G. M. Sheldrick, *Acta Cryst.*, 2015, **C71**, 3–8.
- S4 Olex2 1.5, O. V. Dolomanov, L. J. Bourhis, R. J. Gildea, J. A. K. Howard, H. Puschmann, *J. Appl. Cryst.*, 2009, **42**, 339–341.
- S5 PLATON SQUEEZE: A. L. Spek, *Acta. Cryst.*, 2015, **C71**, 9–18.
- S6 a) C. G. Pierpont, R. M. Buchanan, *Coord. Chem. Rev.*, 1981, **38**, 45–87. b) P. Zanello, M. Corsini, *Coord. Chem. Rev.*, 2006, **250**, 2000–2022. c) W. P. Griffith, *Transition Met. Chem.*, 1993, **18**, 250–256. and references cited therein.
- S7 a) I. Ohkubo, T. Mori, *J. Am. Chem. Soc.*, 2022, **144**, 3590–3602. b) A. Neroni, E. Şaşıoğlu, H. Hadipour, C. Friedrich, S. Blügel, I. Mertig, M. Ležaić, *Phys. Rev. B*, 2019, **100**, 115113.
- S8 H. Matsuura, M. Ogata, K. Miyake, H. Fukuyama, *J. Phys. Soc. Jpn.*, 2012, **81**, 104705.